Global hybrid simulation of mode conversion at the dayside magnetopause

Feng Shi,[1] Yu Lin,[1] and Xueyi Wang[1]

Received 16 April 2013; revised 17 September 2013; accepted 20 September 2013; published 3 October 2013.

[1] Mode conversion at the magnetopause has been suggested to lead to the generation of kinetic Alfvén waves (KAWs) and effective mass transport from the solar wind into the magnetosphere. To investigate the mode conversion process in the dynamic dayside system, a 3-D global hybrid simulation associated with a quasi-parallel shock under a radial interplanetary magnetic field (IMF) is carried out, in which the foreshock compressional pulses are self-consistently generated by the interaction between the solar wind and the geomagnetic field. The results show that as the compressional pulses propagate from the magnetosheath to the magnetopause, short-wavelength structures of $k_\perp \rho_i \sim 0.5$–1 with enhanced parallel electric field $E_\parallel$ are excited in the subsolar magnetopause boundary layer (MPBL), where $k_\perp \simeq k_x$ is the perpendicular waves number nearly along the GSE x direction, and ρ_i is the ion Larmor radius. The wave-phase relationship between the magnetic field and the density changes from in-phase in the magnetosheath to antiphase in the short-wavelength MPBL perturbations. The wave polarization is predominantly compressive in the magnetosheath, whereas strong transverse wave powers appear abruptly around the MPBL. The mode conversion from the compressional pulses to KAWs is identified around the predicted Alfvén resonance surface in the MPBL. As these KAWs evolve, KAW modes dominated by azimuthal wave number with $k_y \rho_i \sim 1$ are also generated. The KAWs in the MPBL are identified by the sharp increases in $E_\parallel$ and the electromagnetic field polarization relations of Alfvén mode, as well as a spectral analysis. The KAW perturbations propagate poleward into the cusps along the MPBL. Due to the differential flow convection speeds at various latitudes, the KAW packets expand along the north-south direction, while they may also merge with newly-formed KAWs due to newly-arrived compressional waves.

Citation: Shi, F., Y. Lin, and X. Wang (2013), Global hybrid simulation of mode conversion at the Dayside Magnetopause, *J. Geophys. Res. Space Physics*, *118*, 6176–6187, doi:10.1002/jgra.50587.

1. Introduction

[2] The Earth's magnetopause boundary layer (MPBL), which separates the shocked solar wind from the magnetosphere, plays a central role in various transport processes involving mass, momentum, and energy from the solar wind into the magnetosphere. Satellite observations exploring this frontier show a very fascinating nature of this dynamic boundary layer. Among various transport processes, reconnection between the interplanetary magnetic field lines and the geomagnetic field lines leads to a direct transport through an "open" boundary at the dayside magnetopause [*Russell and Elphic*, 1978, 1979; *Phan and Paschmann*, 1996; *Phan et al.*, 1996; *Lin and Xie*, 1997; *Fuselier et al.*, 2000; *Hasegawa et al.*, 2002; *Nykyri et al.*, 2006; *Badman and Cowley*, 2007; *Andre et al.*, 2010]. In the cases of a "closed" magnetopause, strong evidence of particle cross-field line diffusion has been brought forward for consideration [*Song et al.*, 1993; *Otto and Fairfield*, 2000; *Johnson et al.*, 2001; *Johnson and Cheng*, 2001; *Chaston et al.*, 2007; *Wang et al.*, 2007]. Wave-particle interaction has been suggested as an important mechanism for the cross-field lines transport at the low-latitude boundary, where large-amplitude ultra-low frequency (ULF) waves are extremely abundant in the geo-observational spectrum [*Tsurutani and Thorne*, 1982; *Anderson et al.*, 1982; *Rezeau et al.*, 1989; *Engebretson et al.*, 1991; *Anderson et al.*, 1994; *Clemmons et al.*, 2000; *Bogdanova et al.*, 2004; *Chaston et al.*, 2008; *Izutsu et al.*, 2012].

[3] Since the plasma density changes inversely with the ambient magnetic field through the MPBL, the Alfvén speed V_A increases dramatically from the magnetosheath to the magnetosphere. This unique feature has led to the suggestion of an interesting ULF wave phenomenon: the mode coupling between the compressional and the Alfvén modes at the location inside the boundary layer where the Alfvén resonance condition $\omega^2 = k_\parallel^2 V_A^2$ is satisfied [*Tamao*, 1965; *Uberoi*, 1972; *Chen and Hasegawa*, 1974; *Southwood*, 1974;

[1]Physics Department, Auburn University, Auburn, Alabama, USA.

Corresponding author: F. Shi, Physics Department, Auburn University, Auburn, AL 36849, USA. (fzs0002@tigermail.auburn.edu)

2169-9380/13/10.1002/jgra.50587

Hasegawa et al., 1983], with ω being the wave frequency and $k_\parallel$ the wave number parallel to the magnetic field. Based on the one-dimensional (1-D) linear theory [*Hasegawa and Chen*, 1974, 1976; *Johnson and Cheng*, 1997], such mode coupling leads to the mode conversion from fast waves to kinetic Alfvén waves (KAWs) [*Hasegawa and Chen*, 1976], which can be solved by kinetic models including finite ion Larmor radius effects. Fast-mode compressional waves frequently arise from the turbulent foreshock of quasi-parallel bow shock [*Lin and Wang*, 2005; *Lin et al.*, 2007; *Wang et al.*, 2009; *Kajdic et al.*, 2011], which in general have $\omega^2 > k_\parallel^2 V_A^2$. The conversion from compressionally to transversally polarized waves provides a source of kinetic-scale Alfvén waves and has been suggested a promising mechanism for an effective plasma heating and transport across the MPBL [*Hasegawa and Mima*, 1978; *Lee et al.*, 1994; *Johnson and Cheng*, 1997; *Chen*, 1999; *Johnson et al.*, 2001; *Johnson and Cheng*, 2001].

[4] Sharp changes in the wave polarization, from compressional in the magnetosheath to transverse in the MPBL, have been observed [*Johnson et al.*, 2001], which provide evidence of the mode conversion. Recent multipoint spacecraft measurements of MPBL crossing substantiate the suggestion of the mode conversion process and the presence of KAWs at the magnetopause [*Chaston et al.*, 2007, 2008; *Yao et al.*, 2011]. The spectrograms in these observations show that the transverse electric and magnetic field components are well correlated with each other, and they match with small-scale KAW dispersion relations. Strong evidence has suggested that these waves with a broadband range in magnetic fluctuations could be characterized by a Doppler-shifted KAW spectrum [*Stasiewicz et al.*, 2001; *Chaston et al.*, 2005]. The dispersion relation of KAWs can be expressed as $\omega = k_z V_A \sqrt{1 + k_\perp^2(\rho_s^2 + \rho_i^2)}$, which leads to the field polarization relation $|\delta E_\perp / \delta B_\perp| \simeq \frac{V_A(1+k_\perp^2\rho_i^2)}{[1+k_\perp^2(\rho_s^2+\rho_i^2)]^{1/2}} \simeq V_A\sqrt{1+k_\perp^2\rho_i^2}$ if $T_e/T_i \ll 1$, where $\rho_s = (T_e/m_i)^{1/2}/\Omega_i$, $\rho_i = (T_i/m_i)^{1/2}/\Omega_i$, Ω_i is the ion-cyclotron frequency, and T_e and T_i are the electron and ion temperatures, respectively. The dispersion relation of KAWs under broader conditions can be found in the recent work of *Bellan* [2012]. A distinct feature of KAWs is the presence of parallel electric field perturbation $\delta E_\parallel$, which is related to the perpendicular electric field perturbation $\delta E_\perp$ as $|\delta E_\parallel| = |\delta E_\perp|(k_\perp\rho_i)(k_\parallel\rho_i)(T_e/T_i)/(1 + k_\perp^2\rho_i^2)$. Observations have also indicated that these KAWs may play a significant role in particle acceleration, heating, and transport through Landau damping, transit time damping, and transverse ion acceleration via demagnetization or stochastic ion scattering on the ion-cyclotron scale field structures [*Chaston et al.*, 1999, 2007, 2008, 2012]. Besides, transport of large cross-field electromagnetic energy across the MPBL have been observed in these observations, which indicate that waves are strong enough to provide an effective particle diffusion coefficient.

[5] Hybrid simulations in two-dimensions (2-D) and three-dimensions (3-D) have been carried out by *Lin et al.* [2010, 2012] for mode conversion at the magnetopause in slab geometries under a steady state, monotonic fast-mode driver. These simulations, which solve the fully kinetic ion physics in a self-consistent electromagnetic field, illustrate how the incoming compressional fast-mode waves are mode converted to short-wavelength KAWs ($k_\perp\rho_i \sim 1$) at the Alfvén resonant surface. This work shows that the behaviors of mode conversion depend on wave frequency, wave vector, Alfvén speed profile, ion β_i in the magnetosheath, electron-to-ion temperature ratio, and the incident wave amplitude. Moreover, the 3-D simulation shows the excitation of KAWs with the perpendicular and azimuthal wave vector component due to the nonlinear physics, which is crucial for large transport across the boundary [*Lin et al.*, 2012]. Strong ion heating in the resulting KAWs is also found in these simulations, consistent with the theories [e.g., *Johnson and Cheng*, 2001] and observations [*Chaston et al.*, 2008].

[6] These previous simulations [*Lin et al.*, 2010, 2012], however, are based on an oversimplified configuration of the MPBL. In the global magnetosphere, the foreshock waves interact with the magnetopause in the form of wave pulses with finite spatial extent and time duration, while the mode conversion as predicted by theories occurs in a highly localized region around the Alfvén resonance points. Realistically, the transient foreshock wave forms the global nonuniformity, and the presence of the background flow convection must be considered to understand the mode conversion and the evolution of the resulting KAWs.

[7] In order to identify the mode conversion process in the global system around the dayside magnetosphere, in this paper, we present a 3-D global-scale hybrid simulation of the dayside magnetosphere associated with a quasi-parallel bow shock. In the previous 3-D global hybrid simulations of *Lin and Wang* [2005], whistler-type electromagnetic waves and compressional waves/pressure pulses generated in the foreshock of the quasi-parallel shock are found to propagate onto the magnetosphere and lead to short-wavelength pulses with enhanced parallel electric field in the magnetopause. In this paper, we present detailed analysis to show that these waves are the KAWs generated by the mode conversion from the compressional pulses.

[8] The outline of the paper is as follows. The simulation model is described in section 2. The simulation results are presented in section 3. The mode conversion is studied by tracking the evolution of wave structures from the magnetosheath to the magnetopause, and the structure of KAWs around the magnetopause. A concluding summary is given in section 4.

2. Simulation Model

[9] The dayside global-scale hybrid simulation model utilized in this study was first developed by *Swift* [1996] and then extended 3-D by *Lin and Wang* [2005]. In the hybrid model, ions are treated as fully kinetic particles, and the electrons are treated as a massless fluid. The ion motions are described by their equation of motion, in the simulation unit,

$$\frac{d\mathbf{v}_i}{dt} = \mathbf{E} + \mathbf{v}_i \times \mathbf{B} - \nu(\mathbf{V}_i - \mathbf{V}_e), \tag{1}$$

where $\mathbf{v}_i$ is the ion particle velocity, $\mathbf{E}$ is the electric filed, $\mathbf{B}$ is the magnetic field, ν is the collision frequency, and $\mathbf{V}_i$ and $\mathbf{V}_e$ are the bulk flow velocities of ions and electrons, respectively. The electric field is obtained from the momentum equation of the electron fluid

$$\mathbf{E} = -\mathbf{V}_e \times \mathbf{B} - \nu(\mathbf{V}_e - \mathbf{V}_i) - \nabla P_e/\mathbf{N}, \tag{2}$$

where P_e is the thermal pressure of the electrons, and N is the electron density or the ion number density based on the assumption of quasi-charge neutrality which is obtained by calculating the zero moment of ions in the particle discrete phase space. The collisional frequency ν, equivalent to resistivity, is set to be nearly zero around the MPBL regions so that the parallel electric field is mainly determined by the electron pressure gradient [*Lin and Wang*, 2005].

[10] The Ampere's law is used to evaluate the electron bulk flow velocity

$$\mathbf{V}_e = \mathbf{V}_i - \frac{\nabla \times \mathbf{B}}{\alpha N}. \tag{3}$$

The magnetic field is updated with Faraday's law

$$\frac{\partial \mathbf{B}}{\partial t} = -\nabla \times \mathbf{E}. \tag{4}$$

[11] For the presentation, the physical quantities are normalized as follows. The magnetic field **B** is scaled by the IMF $\mathbf{B}_0$; the ion number density N by the solar wind density N_0; the time t by the inverse of the solar wind ion gyrofrequency, Ω_{i0}^{-1}; the plasma flow velocity **V** by the solar wind Alfvén speed V_{A0}; the temperature by V_{A0}^2; and the length by the Earth radius R_E.

[12] Spherical coordinates are adopted in our 3-D simulation, and the same as *Lin and Wang* [2005] and *Tan et al.* [2012]. The simulation domain contains the system of the bow shock, magnetosheath, and magnetosphere in the dayside region with GSM $x > 0$ and a geocentric distance $4\ R_E \le r \le 22\ R_E$. The Earth is located at the origin $(x, y, z) = (0, 0, 0)$. Outflow boundary conditions are utilized at $x = 0$, while inflow boundary conditions of the solar wind are applied at $r = 22\ R_E$. The inner boundary at $r = 4\ R_E$ is assumed to be perfectly conducting, and an additional cold ion fluid is used to model the inner magnetosphere at $r < 7\ R_E$.

[13] A radial IMF is assumed for the case shown in this paper, with $B_{x0} = -1$, $B_{y0} = 0$, and $B_{z0} = 0$. The ion inertial length in the solar wind is chosen as $d_{i0} = 0.1\ R_E$. A uniform solar wind plasma with ion beta value $\beta_i = 0.5$ and Alfvén Mach number $M_A = 5$ is employed, which flows into the system along the $-x$ direction with an isotropic drifting Maxwellian distribution. A total of about 4×10^8 particles are used, and the number density of the macro-ion particles is set to be $N_0 = 11,000\ R_E^{-3}$ in the solar wind. An isothermal electron equation of state is assumed, with $\beta_e = 2.0$ in the solar wind plasma to ensure a temperature ratio $T_e/T_i \simeq 0.1$–0.2 at the magnetopause.

[14] Nonuniform grid spacing is used in the radial direction, with a higher resolution of $\Delta r = 0.05 R_E$ around the magnetopause in order to identify the small-scale KAWs, while $\Delta r = 0.1\ R_E$ to $0.14\ R_E$ in the solar wind and magnetosheath regions. Note that hybrid models are valid for low-frequency physics up to $\omega \sim \Omega_i$ and $k\rho_i \sim 1$ (wavelength $\sim 6\rho_i$). The finite ion gyroradius effects are resolved with time steps much smaller than the gyroperiod. The grid sizes used in this simulation are small enough to resolve the waves in the foreshock, where the ion Larmor radius is determined by the shock heated ions, as well as the magnetopause waves. These grid sizes result in about 150–300 particles per cell in and upstream of the bow shock, and about 60–100 particles per cell (or at least 15,000 particles within a wavelength scale) in the region around and on the sunward side of the Alfvén resonance surface at the magnetopause, where the resulting waves and the mode conversion are present. Increasing the particle number density is found not to change the physical results. A total grid of $N_r \times N_\phi \times N_\theta = 180 \times 104 \times 130$ is used. The time step to advance the positions of particles is $0.05\Omega_{i0}^{-1}$.

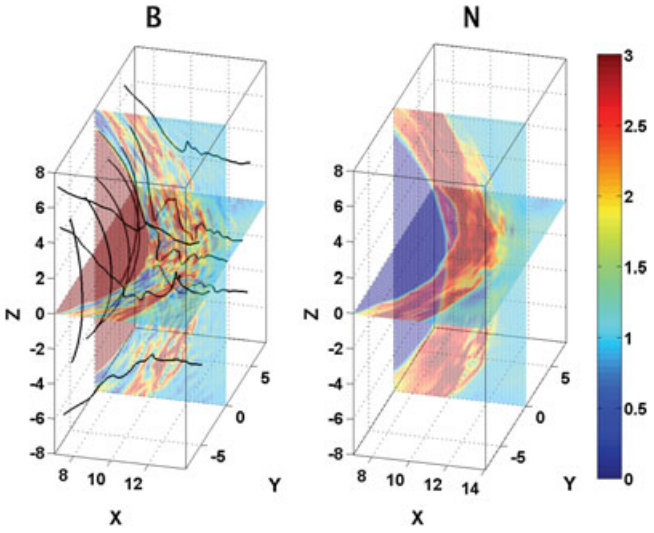

Figure 1. Spatial contours of magnetic field strength B and ion density N at $t = 150$ showing the 3-D structures of self-consistently generated bow shock and magnetopause, as well as the compressive pulses in the magnetosheath. Typical field lines are also shown in the magnetic field plot.

3. Simulation Results

3.1. Overall Structure

[15] Figure 1 shows contours of the magnetic field strength B and ion density N in the noon meridian and equatorial planes at $t = 150$. Typical magnetic field lines in the 3-D perspectives are also displayed in the magnetic field contours. The self-consistently generated bow shock is saturated around a standoff radial distance of $12\ R_E$ at $t = 40$, while the magnetopause is roughly at $10\ R_E$ in the subsolar region. Compressional pulses in B and N and transverse magnetic field perturbations are present in the magnetosheath, which surrounds the magnetosphere and located in the region between the bow shock and magnetopause. The wave perturbations are mainly due to the turbulence in the bow shock and foreshock region generated by backstreaming ions in the foreshock of the quasi-parallel shock [*Lin and Wang*, 2005], which is around the low-latitude regions with $|z| < 3\ R_E$, and are carried earthward by the shocked solar wind plasma. Specifically, the shock front could be identified from the earthward enhanced magnetic field and ion density. The magnetopause can be distinguished through the sharply increased (decreased) magnetic field (ion density) toward the Earth downstream of the bow shock. In addition to the compressional pulses, diamagnetic

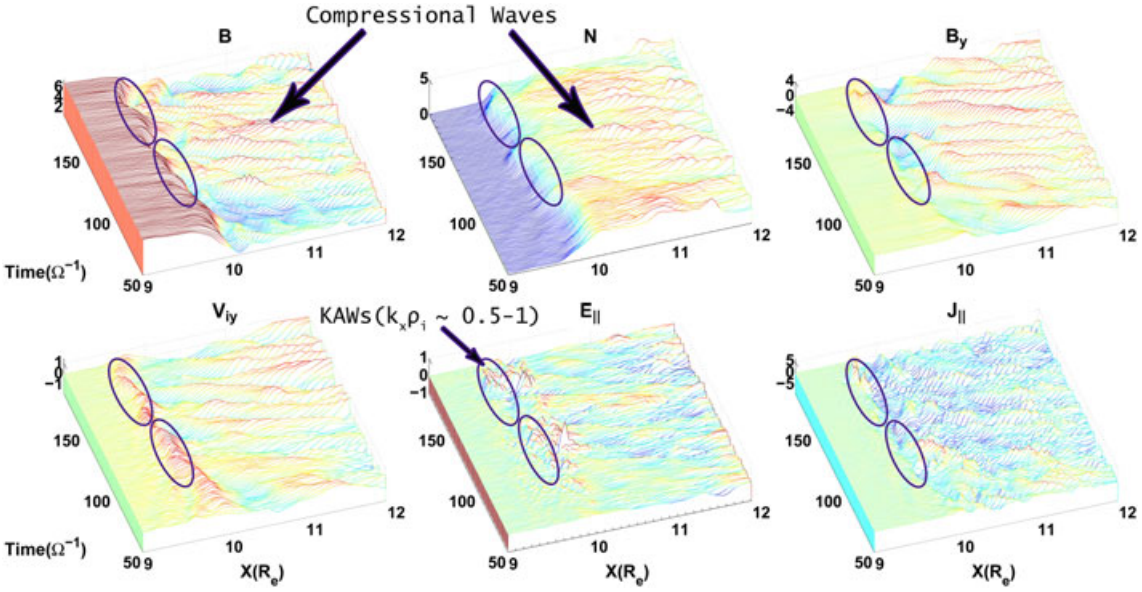

Figure 2. Time evolution of spatial profiles of various quantities along the Sun-Earth line during the time interval t = 50–180. The circles highlight areas with locally excited $E_{||}$ around the MPBL, which are shown to be KAW structures in later sections.

cavities with decreased magnetic field and density are also generated in the foreshock (not shown here) and propagate through the magnetosheath. The foreshock compressional waves develop into elongated structures along the field lines, with wave vectors $k_\perp \gg k_{||}$. The dynamics and evolution of the fast-mode/whistler compressional waves and diamagnetic cavities have been simulated in great details [*Lin and Wang*, 2005; *Blanco-Cano et al.*, 2009; *Kajdic et al.*, 2011].

[16] Figure 2 illustrates the spatial profiles of various quantities along the Sun-Earth line in a time sequence from t = 50–180. The incoming fast-mode compressional wave pulses with perturbations of B and N constantly propagate onto the magnetopause. The oscillating MPBL can be identified from the sharp increase of B and decrease of N around x = 9.9 R_E. Note that the bow shock is located near 12 R_E and not shown in Figure 2. Specifically, the fast-mode waves generated near the bow shock at about t = 100 propagate onto the MPBL at a later time about t = 120. The typical Alfvén speed is about 1.4 V_{A0} around 11 R_E in the magnetosheath outside the MPBL. At this location, the compressional waves are seen to propagate sunward with a speed about 2–3 V_{A0} in the plasma frame, while the earthward and azimuthal plasma convection speed is about 5 V_{A0}, giving a net wave propagation speed of ~ 2–3 V_{A0} in the simulation (Earth) frame of reference. Near the magnetopause at $x \simeq$ 10.5 R_E, the x-component velocities of these wave pulses are significantly slowed down. The compressional pulses then consequently impinge on the magnetopause obliquely. In addition, the transverse perturbations can be seen from the profiles of B_y and ion flow velocity V_{iy}.

[17] When the series of wave packets interact with the magnetopause, strong perturbations in the parallel electric field $E_{||}$ are excited near and inside (shown in circled regions) the MPBL transition, from $t \simeq$ 120–140 and 160–180. These excited waves are dominated with short wavelengths of $k_x\rho_i \sim$ 0.5–1. Meanwhile, perturbations in the parallel current $J_{||}$, B_y, and V_{iy} are also evident near the magnetopause region. These correlated perturbations can be considered a good indicator of possible signature of KAWs based on the linear theory of mode conversion at the MPBL with the normal nearly along x. In the following, we present a detailed identification of the mode conversion from compressional to transversely dominated KAWs.

3.2. Conversion From Compressional Waves in the Magnetosheath to Transverse Waves in the MPBL

[18] Figure 3 presents the spatial contours of magnetic field components B_x and B_y, field strength B, ion density N, ion bulk flow velocity components V_{ix}, V_{iy}, and V_{iz}, and parallel current $J_{||}$ in the equatorial plane at t = 150. In this figure, the magnetopause can be identified from the sharp changes in B and N as described above. Wave structures are seen in r > 10 R_E in the magnetosheath, with wave fronts largely perpendicular to the magnetopause boundary normal. Meanwhile, wavy motions are produced at the magnetopause due to the arrival of the compressional waves. The three circles at y = 5 R_E, y = 0 (subsolar region), and y = –5 R_E in each plot of Figure 3 mark the regions of strongly distorted magnetopause. Large-amplitude perturbations are seen in B_y, V_{iy}, V_{iz}, and $J_{||}$ in these magnetopause surface waves together with moderate perturbations in B_x and V_{ix} as well as in N and B. These waves propagate eastward and westward away from the subsolar area along the magnetopause.

[19] To understand the dynamical interaction between the foreshock/magnetosheath waves and the magnetopause, Figures 4a and 4b depict time variations of B and N along the sun-earth line at fixed positions x = 9.8 R_E and x = 11.8 R_E, respectively. Figure 4a shows that at earlier times before t = 80, when B is high and N is low, the location x = 9.8 R_E is on the magnetospheric side in MPBL. As time goes on, the magnetopause sweeps through this location three times, as seen from the oscillating B and N, so that it is on the magnetosheath side at $t \simeq$ 180. The oscillating

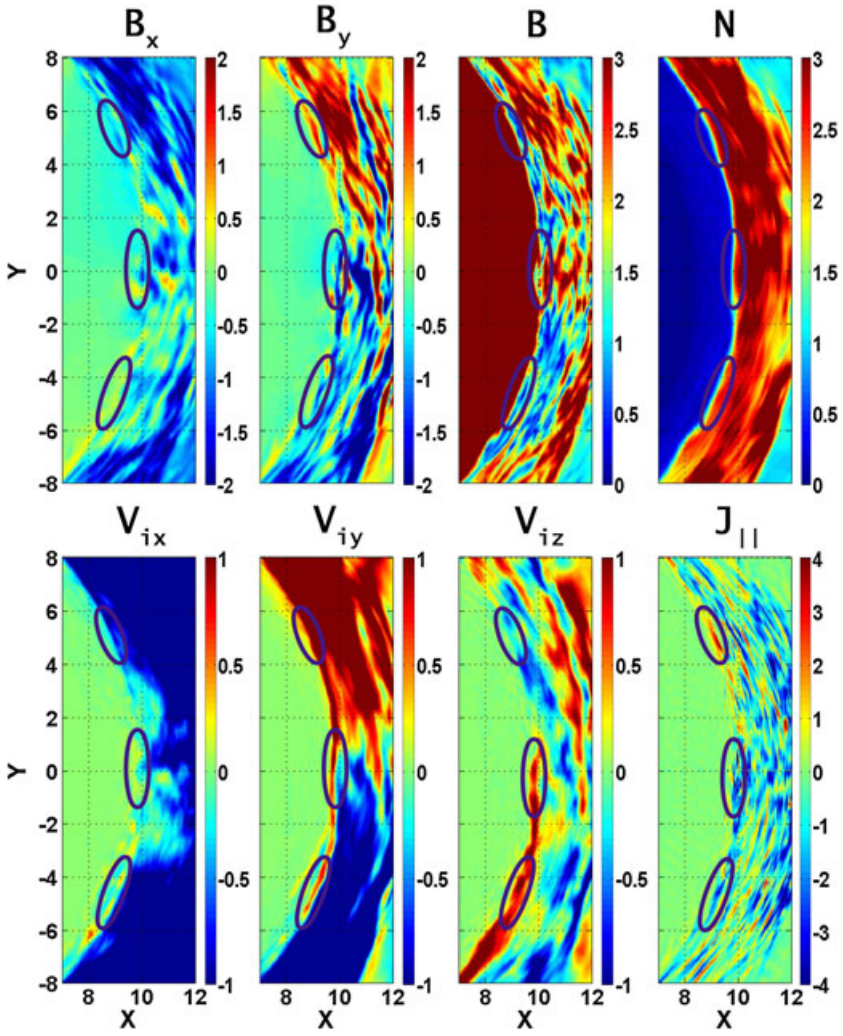

Figure 3. Contours of various quantities in the equatorial plane at t = 150. The three circles at y = –5, 0, 5 R_E in each plot spot the strong perturbations round the MPBL.

magnetopause results in the background low frequency, antiphase oscillations in B and N. Meanwhile, a remarkable feature is that the high-frequency oscillation structures in Figure 4a also denote an antiphase relation between B and N. Therefore, the MPBL is dominated by the antiphase relation between the magnetic field and the density. On the other hand, the location x = 11.8 R_E in Figure 4b is always in the magnetosheath. No background low-frequency oscillation is found here. The perturbations are of high frequency, dominated by an in-phase relation between B and N but also mixed with a few antiphase structures. Overall, the wave polarization changes distinctively from a predominantly in-phase relation between B and N in the magnetosheath to an antiphase relation in the MPBL.

[20] The power spectra of the transverse (B_y) and compressional (B) components of the magnetic field, as a function of x at (y, z) = (0.0, –1.0) R_E, are shown in Figure 5. The frequency ω, normalized by the solar wind Ω_{i0}, at various locations is obtained from the simulation data in the time duration from t = 62–190. During this time interval, the bow shock is oscillating around x = 12 R_E, and the magnetopause is around x = 9.8 R_E. The magnetosheath is occupied predominantly by compressional waves, whereas relatively weak transverse wave power is also present. These waves propagate toward the magnetopause, while they are Doppler-shifted in the simulation (Earth) frame of reference due to the magnetosheath flows, which are spatially dependent. The compressional wave power in the magnetosheath is of broadband, from ω = 0.1–1.0. Around the MPBL from x = 9.6–10.0 R_E, however, significant transverse wave powers appear abruptly, with a spectral width of ω = 0.2–0.4. These transverse waves exist in the same region where B and N have an antiphase relation, as discussed in Figure 4a.

[21] Note that the strong compressional wave power in the MPBL in low frequencies of $\omega \sim$ 0.1–0.2 is caused by the oscillation of the magnetopause. Wave powers at a very low frequency, $\omega <$ 0.1, are present in both the compressional and transverse oscillations, and in both the magnetosheath and the magnetopause. These powers are caused by a systematic motion of the entire regions of the magnetosheath and magnetopause. The antiphase relation between the magnetic field and the density, the dominance of the broadband transverse wave powers in the MPBL, and the excitation of the parallel electric field (shown in Figure 2) appear to be

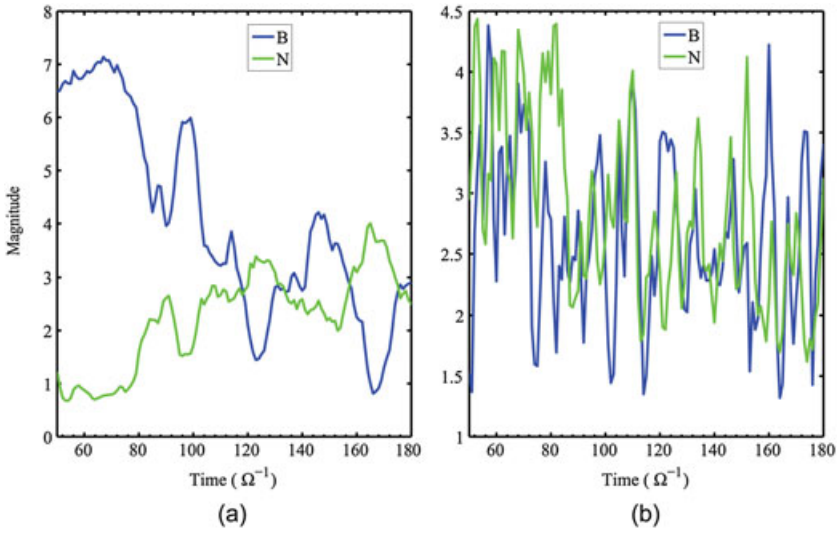

Figure 4. Time variations of B and N at two locations along the sun-earth line: (a) antiphase relation at $x = 9.8\ R_E$ in the MPBL, and (b) predominantly in-phase relation at $x = 11.8\ R_E$ in the magnetosheath.

consistent with the presence of kinetic Alfvén waves through a mode conversion from the compressional waves.

3.3. Identification of the Mode Conversion and Generation of KAWs

[22] To further pinpoint the dynamical mode conversion process that may have occurred in the MPBL, we now present a detailed analysis of wave structures around the MPBL. Figure 6 shows the spatial cut of physical quantities B, N, B_y, $E_\parallel$, and $J_\parallel$ through the magnetopause region along the sun-earth line at $t = 163$, where the magnetic field decreases and the density increases from $x = 9.5 - 10\ R_E$. Correspondingly, the local Alfvén speed V_A increases approximately from 0.5 to 9.9 V_{A0} from $x = 10 - 9.5\ R_E$ inward.

[23] The parallel wavelength of incoming waves from the magnetosheath is measured to be 3–8 R_E approximately, which corresponds to $k_\parallel \rho_i \sim 0.04$–$0.1$, where $\rho_i \sim 0.5 d_{i0}$ is the local ion Larmor radius. The perpendicular wavelength in x direction is about 0.2–0.5 R_E, corresponding to $k_x \rho_i \sim 0.5$–1. The ion gyrofreqency Ω_i is about 4–$5\Omega_{i0}$ at the magnetopause, while the dominant incident wave frequency ranges from 0.2–$0.5\Omega_{i0}$, as discussed in Figure 5, and thus $\omega^2/\Omega_i^2 \ll 1$. The incident wave has $\omega > k_\parallel V_A$, as described

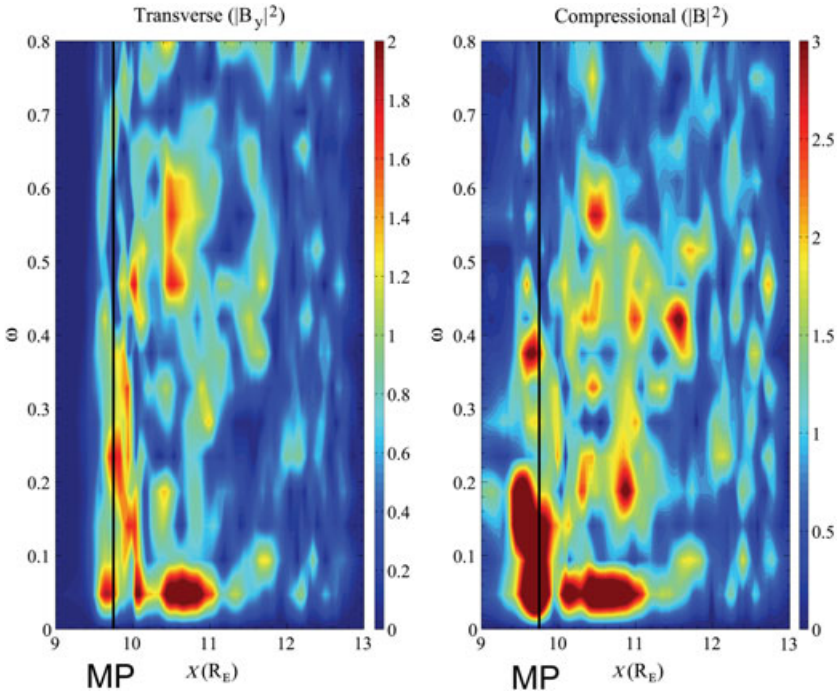

Figure 5. Power spectra of transverse and compressional components as a function of x at $(y, z) = (0.0, -1.0)\ R_E$.

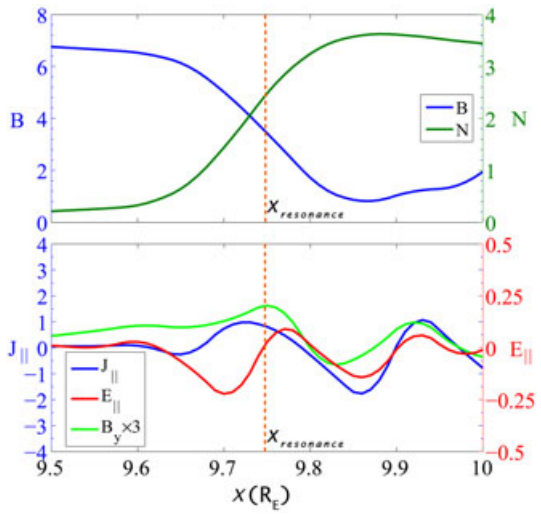

Figure 6. Spatial cuts of various quantities through the MPBL along sun-earth line at t = 163. The vertical dotted lines mark the average location of the predicted Alfvén resonance point.

in section 3.1. For the average dominant $\omega \sim 0.3\Omega_{i0}$ as measured in the MPBL to be consistent with the frequency due to the mode conversion, the Alfvén resonance condition for the subsolar locations with nearly a zero flow convection speed, $\omega = k_{||} V_A(1 - \omega^2/\Omega_i^2) \simeq k_{||} V_A$, requires $V_A \simeq 2.2\ V_{A0}$. This value of the Alfvén speed corresponds to $x \simeq 9.75\ R_E$ as V_A ramps up into the MPBL, as indicated by the yellow vertical line in Figure 6.

[24] The spatial profiles of physical quantities around the MPBL confirm the existence of the predicted Alfvén resonance point. Around this average location of the predicted Alfvén resonance point, $E_{||}$ is strongly enhanced, as seen in Figure 6, and it then shows a purely decay spatial profile on the magnetospheric side, consistent with theories of the mode conversion [*Hasegawa and Chen*, 1976]. The waves propagate back to the magnetosheath side. Similar behaviors are seen in $J_{||}$ and B_y. The correlation of these quantities are consistent with the KAW structures dominated by k_x in the analytical theory [*Hasegawa and Chen*, 1976] and previous hybrid simulations of mode conversion for a local magnetopause [*Lin et al.*, 2010, 2012].

[25] The mode-converted Alfvén mode waves can be identified by examining the wave polarization relation. Suppose a background magnetic field pointing in the z direction and a KAW with the wave vector **k** in the xz plane, as seen above for the mode structures along the normal of the subsolar MPBL. The wave polarizations in Alfvén waves with $k_\perp = k_x$ are dominated by perturbations in B_y and E_x. Based on the kinetic theory, $\delta E_x = V_A \delta B_y \left\{1 + T_e/T_i[1 - I_0(\lambda_i)e^{-\lambda_i}]\right\}$ in the KAW, where $\lambda_i = k_x^2\rho_i^2$, and $I_0(\lambda_i)$ is the modified Bessel function of the first kind. In our simulation, $k_x\rho_i \approx$ 0.5–1, the averaged $T_e/T_i \approx 0.2$ at the magnetopause, and thus $\delta E_x \simeq \sqrt{1 + k_\perp^2\rho_i^2} V_A \delta B_y \simeq 1.1 V_A \delta B_y$ is required for KAWs based on the Pade approximation. Figure 7 presents the results at t = 150 in the xz plane due to the arrival of pressure pulses at the MPBL. Figure 7a shows the contours of $E_{||}$, in which the enhancement of the parallel electric field in the MPBL is highlighted with the circled region. Consistent with the theoretical prediction for KAWs, the waves in the MPBL are found to be dominated by δB_y and δE_x. Figure 7b shows δE_x versus δB_y for all the MPBL points inside this circle, with the violet dashed lines marking the polarization relation $\delta E_x = \pm 1.1 V_A \delta B_y$ for KAWs around the subsolar MPBL. The perturbed quantities δB_y and δE_x are defined relative to the "equilibrium" values after t = 50, which are calculated by taking the average field values over data time duration from t = 50–150. Here, V_A is the local Alfvén speed based on the equilibrium magnetic field and density. It is seen from Figure 7 that the Alfvén mode polarization relation is nearly satisfied in the circled region. For majority regions outside the MPBL, however, the relation is found to be poorly satisfied.

[26] The signs of slope of the solid lines in Figure 7b represent the direction of the Alfvén mode propagation along z, which is nearly the direction of the magnetic field lines. In this case, the wave structures in the MPBL obtained from the simulation consist of two parts: the positive slope for $z > 1.1\ R_E$, indicating a wave branch traveling northward along the field lines, and the negative slope for $z < 1.1\ R_E$, denoting another branch propagating southward along the field lines. This result is in agreement with our expectation that pulses coming onto the MPBL would break up into two parts that propagate to the opposite directions along the field lines.

[27] The polarization relation of the waves with an enhanced parallel electric field, again marked by circles, in the equatorial MPBL is shown in Figure 8 for t = 150 (top row) and t = 163 (bottom row). The Alfvén mode polarization relation is again nearly satisfied in these waves. The waves in this plane are seen to propagate either

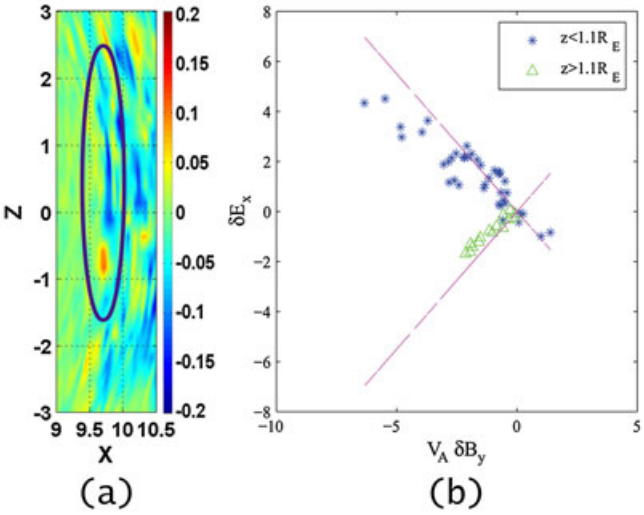

Figure 7. (a) Spatial profile of $E_{||}$ around the MPBL in the noon-meridian plane at t = 150. (b) Corresponding polarization relation at the spatial points inside the circled regions in Figure 7a showing Alfvén modes propagating in the opposite directions along the field lines. The violet dashed lines in Figure 7b denote the theoretically predicted polarization relation $\delta E_x = \pm 1.1 V_A \delta B_y$ for the KAWs.

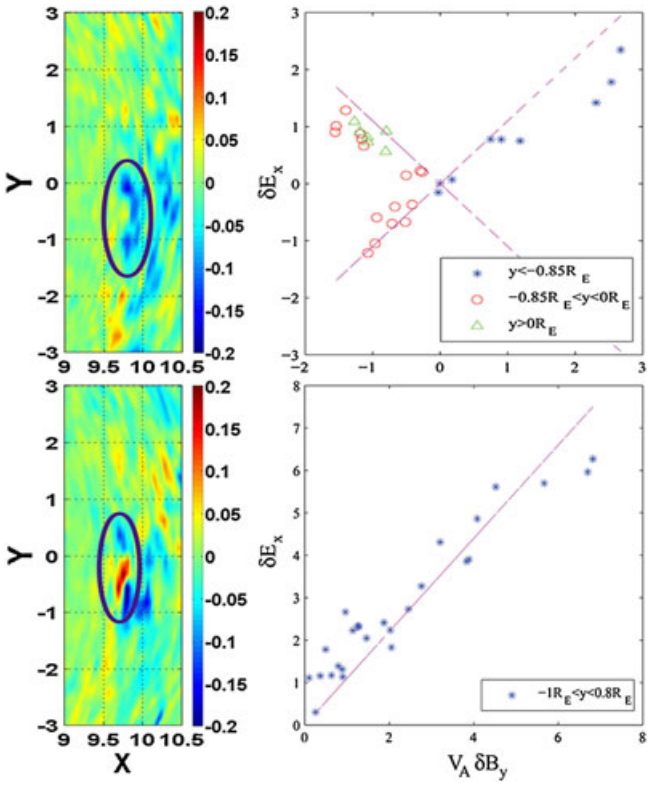

Figure 8. (top left) Spatial profile of $E_{\parallel}$ around the MPBL in the equatorial plane at t = 150. (top right) Corresponding polarization relation in the circled regions on the top left showing Alfvén modes propagating in different directions along the field lines. (bottom left) Spatial profile of $E_{\parallel}$ around the MPBL in the equatorial plane at t = 163; (bottom right) corresponding polarization relation in the circled regions in Figure 8 (bottom left) showing Alfvén modes. The violet dashed lines in Figure 8 (left column) represent the theoretically predicted polarization relation $\delta E_x = \pm 1.1 V_A \delta B_y$ for the KAWs.

northward or southward. Specifically, at t = 150, the wave structures in the region with –1.5 $R_E < y <$ –0.85 R_E have a positive slope in the δE_x-δB_y plot and thus propagate northward. In the region with –0.85 $R_E < y < 0$, both positive and negative slopes are seen, and the Alfvén mode waves propagate either northward or southward. In the region with $0 < y <$ 0.3 R_E, the waves propagate southward along the field lines. At t = 163, strongly enhanced $E_{\parallel}$ is again present in the MPBL, as shown in Figure 8 (bottom left), due to the arrival of a new pressure pulse. These Alfvén waves now propagate northward with the Alfvén speed, as shown in Figure 8 (bottom right).

3.4. Generation and Identification of KAWs Dominated by the Azimuthal Wave Numbers

[28] Besides the features described above, the $E_{\parallel}$ structure is seen to have clearly evolved into waves with a large $k_y\rho_i \sim 0.4$ at the later time of t = 163 in Figure 8. The presence of large azimuthal wave numbers k_y is crucial to the particle transport across the field lines. *Lin et al.* [2012] have found with simulations of a local slab magnetopause boundary that following a stage dominated by the linear physics of mode conversion, which leads to the excitation of KAWs with large k_x, perpendicular and azimuthal $k_y\rho_i$ are generated in the nonlinear stage when the amplitude of KAWs generated by linear mode conversion becomes large enough to drive a nonlinear parametric decay process.

[29] Since the plasma and magnetic field are nearly uniform in the azimuthal direction in the subsolar MPBL, a spectral analysis can be easily performed by Fourier transform in the k_y space. Thus, to further test the dependence of the wave polarization on the wave number, we now analyze the wave spectrum of $E_{\perp}(k_{\perp})/B_{\perp}(k_{\perp})$ from our simulation and compare it with the polarization relation based on the analytical theory of KAWs. The test is performed for the azimuthal k_y modes along a line segment at x = 9.82 R_E from 3 $R_E \le y \le$ 3 R_E, which is located inside the subsolar MPBL. In these modes dominated by k_y, the transverse polarization of the electromagnetic field is dominated by δE_y and δB_x. The dots in Figure 9 show the dependence of $E_y(k_y)/B_x(k_y)$ on k_y obtained from the simulation at t = 150, where $E_y(k_y)$ and $B_x(k_y)$ are the Fourier spectra of E_y and B_x. The analytical relation, $E_y/B_x \simeq V_A\sqrt{1+k_y^2\rho_i^2}$ for KAWs dominated by $k_{\perp} = k_y$ in this case with $T_e/T_i \ll 1$, is also denoted by a green line in Figure 9, where the values of the average background Alfvén speed, V_A, at the local line segment are marked at $k_y \sim 0$. The results show a consistency between the simulation and the analytical theory. The predominant wave power in the simulation is found to be in the range of $k_y\rho_i \sim$ 0.3–1. At the higher wave number with $k_y\rho_i \sim 1$ or larger, the waves exhibit the characteristics of KAW modes, whereas at small $k_y\rho_i$ the modes approach the MHD shear Alfvén wave. The results are also consistent with satellite observations of KAWs at the magnetopause [e.g., *Chaston et al.*, 2007, 2008; *Yao et al.*, 2011], in which $k_{\perp}$ is typically inferred from measurements as a Doppler-shifted frequency using the Taylor hypothesis so

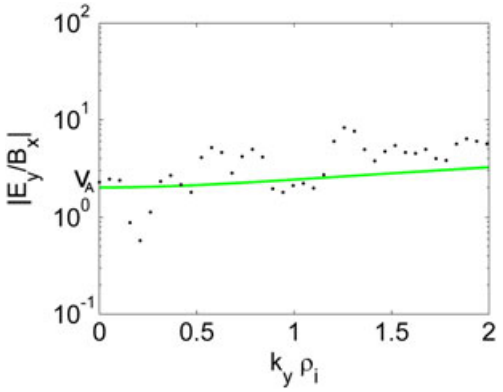

Figure 9. The dots show the wave spectrum of $E_y(k_y)/B_x(k_y)$ as a function of k_y for the azimuthal k_y modes of KAWs obtained from the simulation at x = 9.82R_E and –3$R_E \le y \le$ 3R_E within the equatorial subsolar MPBL at t = 150. The analytical relation $E_y/B_xV_A \sim \sqrt{1+k_y^2\rho_i^2}$ is denoted as the green line. The value of the local average background Alfvén speed is marked on the figure at $k_y \sim 0$.

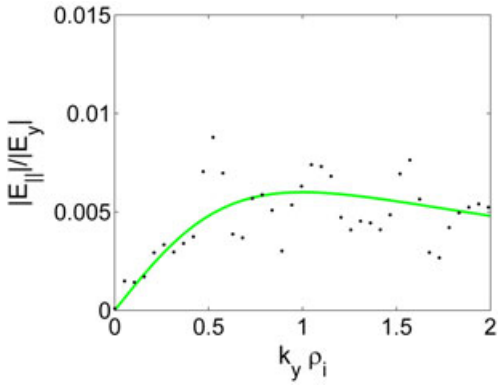

Figure 10. Ratio of $|E_{\|}(k_y)|/|E_y(k_y)|$ for the azimuthal k_y modes of KAWs in the subsolar MPBL, along the same line adopted in Figure 9, at t = 150. The dots are obtained from the simulation, and the green line indicates the relation $(k_y\rho_i)(k_z\rho_i)(T_e/T_i)/(1+k_y^2\rho_i^2)$ obtained from the two-fluid linear theory.

that a plot of the frequency spectrum shows that the wave becomes electrostatic at higher frequency.

[30] In order to determine whether the magnitude of the excited $E_{\|}$ is consistent with that predicted by theories of mode conversion, the dots in Figure 10 depict the ratio $|E_{\|}(k_y)|/|E_y(k_y)|$ as a function of k_y obtained from the simulation for the same line segment as that exploited to obtain Figure 9. Note that the modes dominated by k_x due to the linear mode conversion have $k_y = 0$ [*Lin et al.*, 2010], whereas the $k_y = 0$ modes are excluded in Figure 10. The analytical relation, $|\delta E_{\|}|/|\delta E_{\perp}| = (k_{\perp}\rho_i)(k_{\|}\rho_i)(T_e/T_i)/(1+k_{\perp}^2\rho_i^2)$, based on the two-fluid linear theory [*Hasegawa and Chen*, 1976; *Streltsov et al.*, 1998; *Cheng and Johnson*, 1999; *Hollweg*, 1999] is denoted by the green line in Figure 10, where $E_{\perp} = E_y$ for these modes dominated by $k_{\perp} = k_y$. It is found that the strength of the parallel electric field obtained from the simulation is in good agreement with that of the KAWs predicted by the theory. Such result is also consistent with the previous hybrid simulation of mode conversion [*Lin et al.*, 2010].

[31] In addition, by comparing the values of $E_{TD} = -\left[m_i v_{i\perp}^2/(2\bar{B})\right] ik_{\|}B_{\|}(k_y)/e$ and $E_{LD} = E_{\|}(k_y)$ (with $\bar{B}$ being the background magnetic field strength), which represent the effective parallel electric field associated with the transit time damping and the Landau damping based on the quasilinear theory [e.g., *Chaston et al.*, 2008], respectively, we find that the magnitude of the transit time damping is roughly 4–8 times of that of the Landau damping, consistent with theories [e.g., *Hollweg*, 1999] and observations [e.g., *Chaston et al.*, 2008]. Moreover, the previous theoretical study of *Johnson and Cheng* [1997] has also indicated that magnetic drift effects contribute significantly to the diffusion coefficient in the mode conversion at the magnetopause. Detailed analysis on ion cross-field line diffusion in the mode conversion in our simulation is beyond the scope of this paper. Our examination also shows that the presence of $\delta B_{\|}$, which is in an antiphase relation with δN as seen in Figure 4, is consistent with the total pressure balance, $\delta B_{\|}/\bar{B} = -\mu_0\delta P_i/\bar{B}^2 = -\mu_0(T_0\delta N_i)/\bar{B}^2$, in this high beta plasma. Consider the quasi-charge neutrality for $\omega^2 \ll k_{\perp}^2 V_A^2$ in KAWs. With the density perturbation $\delta N/N_0 = (ie/k_{\|})\,\delta E_{\|}/T_e$ in the KAWs [*Hasegawa and Chen*, 1976; *Chaston et al.*, 2012], the pressure balance leads to $\delta B_{\|}/\bar{B} \sim (-\beta_i/2)\left[(k_y\rho_i)^2/(1+(k_y\rho_i)^2)\right]\left[ie\delta E_y/(k_y T_i)\right]$, which is nearly satisfied in our simulation for the predominant spectral range $k_y\rho_i \sim 0.3$–1.

[32] Simply put, based on the wave polarization relation and spectral analysis in sections 3.3 and 3.4, the simulation has demonstrated that the resulting waves in the MPBL due to the mode conversion from the compressional pulses are indeed kinetic Alfvén mode waves.

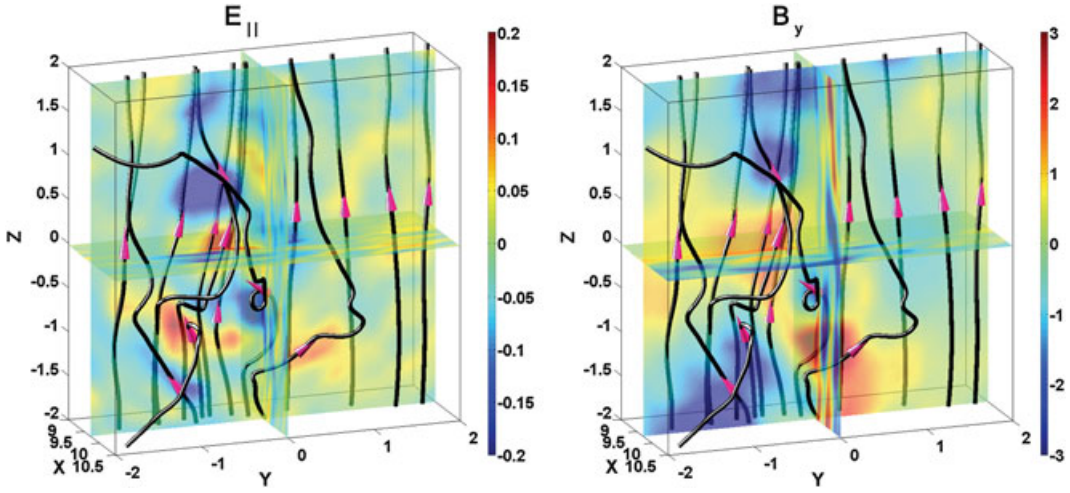

Figure 11. Contours of $E_{\|}$ and B_y around the subsolar region at t = 163, for equatorial plane (z = 0) between x = 9 R_E and 10.5 R_E and y = –2 R_E and 2 R_E, the noon-meridian plane (y = 0) between x = 9 R_E and 10.5 R_E and z = –2 R_E and 2R_E, and the plane with x = 9.75 R_E. Typical magnetic field lines within this region are also plotted, with arrows indicating the field directions.

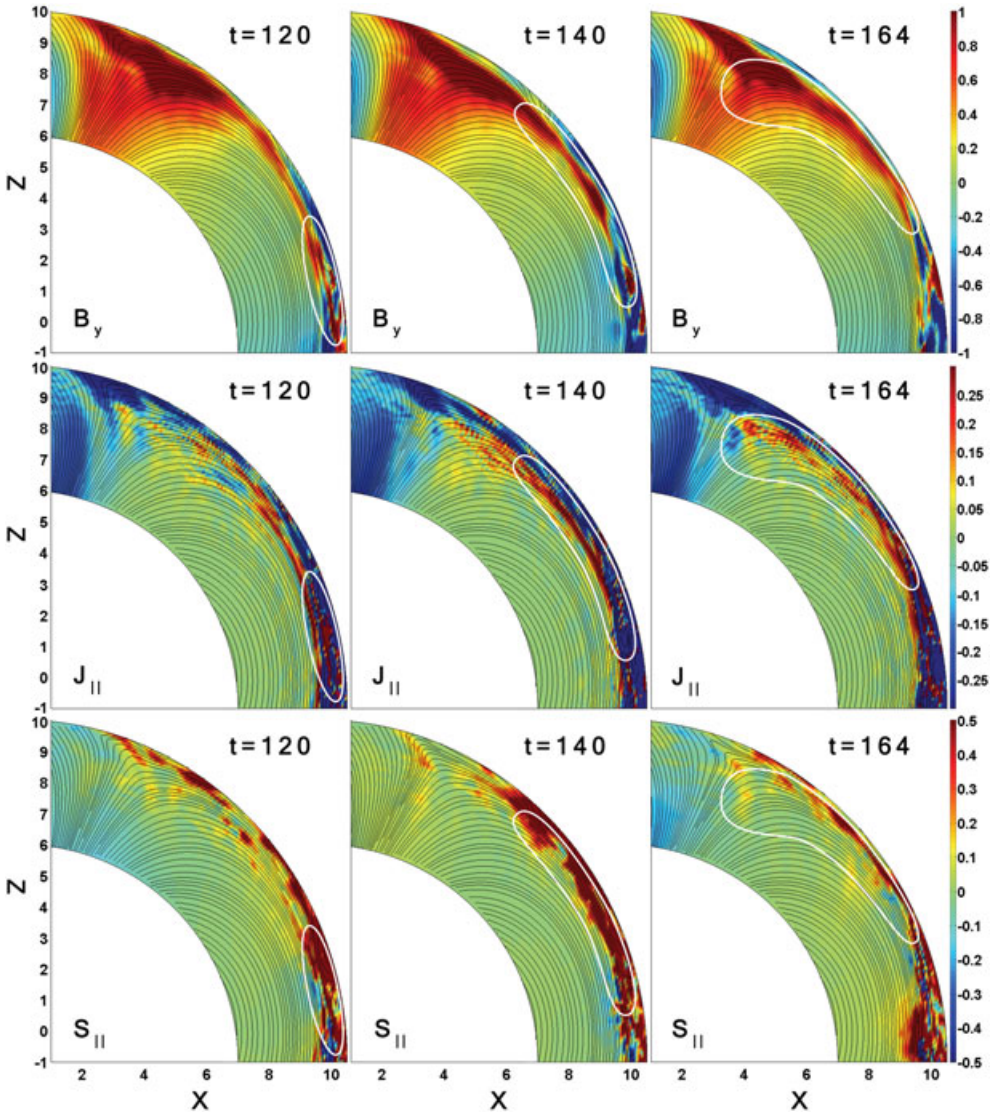

Figure 12. Contours of (top row) B_y, (middle) $J_{\|}$, and (bottom) the field-aligned Poynting flux $S_{\|}$ at three different times t = 120, 140, and 164 in the noon-meridian plane around the magnetopause boundary, from r = 6 R_E to 10 R_E. The sequential propagation of a group of KAWs is tracked with the circled regions.

3.5. Global Distribution and Poleward Propagation of the Alfvén Waves

[33] In order to examine the longitudinal and latitudinal global structures associated with the mode conversion, we plot $E_{\|}$ and B_y around the subsolar region at t = 163 in Figure 11. The contours are shown for equatorial plane (z = 0) between x = 9R_E and 10.5R_E and y = –2R_E and 2R_E, the noon-meridian plane (y = 0) between x = 9R_E and 10.5R_E and z = –2R_E and 2R_E, and the plane with x = 9.75R_E. Typical magnetic field lines within this region are also plotted, with arrows indicating the field directions. At this moment, more pressure pulses hit the dusk side of y = 0 than the dawn side, leading to strongly correlated perturbations in the parallel electric field and the azimuthal magnetic field perturbations. A transition from the magnetosheath-like field lines to the dipole-like lines (ordered and predominantly northward) is observed. The Alfvénic transverse kinks in the field lines are pronounced in the regions with the enhanced perturbations in $E_{\|}$ and B_y. These perturbations are carried away from subsolar area by the convective flows.

[34] Finally, we discuss the poleward movement of Alfvén waves originating from the subsolar region due to the mode conversion. The northward propagation of KAWs will be focused. The subsolar region is abundant of compressional drivers in front of the magnetopause. As a result, KAWs continuously form in the subsolar area, i.e., downstream of the quasi-parallel shock. They are seen to propagate along the field lines down to the cusp region.

[35] Figure 12 shows the contours of B_y, $J_{\|}$, and the field-aligned Poynting vector $S_{\|}$ at three different times (t = 120, 140, and 164) in the noon-meridian plane around the magnetopause boundary, from r = 6 R_E to 10 R_E, where $S_{\|}$ = $(\delta\mathbf{E} \times \delta\mathbf{B}) \cdot \mathbf{b}$, and $\mathbf{b} = \mathbf{B}/B$. The sequential propagation of a group of KAWs is tracked with circled regions in Figure 12. At t = 120, a compressional pulse has come onto the magnetopause, and meanwhile strong perturbations in B_y, $J_{\|}$, and

$S_\parallel$ are seen from $z = -0.5\ R_E$ to $z = 1.5\ R_E$ around the magnetopause, inside the circled subsolar region in the left column. Another strong perturbation (starting with magnetic pulses at an earlier time $t \simeq 114$) from $z = 1\ R_E$ to $z = 3\ R_E$ can be distinguished in the northern part of the circled region as well. The quantities B_y, $J_\parallel$, and the positive (poleward) $S_\parallel$ are well correlated in these KAWs. The propagation speeds, indicating the group speed of the wave packets, of both the leading and trailing edges of the white circle in this subsolar region with an ignorable flow convection are estimated at about V_A in the Earth frame, as expected for the Alfvén modes. KAW perturbations formed at earlier times can also be seen ahead of the KAWs tracked in the higher latitudes along the magnetopause. For a typical IMF of 10 nT and a solar wind density of 5/c.c., our estimation of $S_\parallel$ is $\sim 1.4 \times 10^{-5}$W/m^2 averaged over the wave packet period, consistent with the observations of *Chaston et al.* [2007].

[36] At $t = 140$, the circled region is elongated and expands along the magnetopause due to the larger background convection speed of the leading edge as it moves to a higher latitude, as seen in the middle column of Figure 11. The B_y perturbations in the middle part of these KAWs thus appear weaker due to the expansion, at $z \simeq 4.5\ R_E$. But the trailing part is then merged with KAWs generated by some newly arriving pressure pulses. Enhancement of the local perturbations in B_y and $J_\parallel$ appear at $z \simeq 2.5\ R_E$. Enhanced poleward $S_\parallel$ again exists correspondingly. The speed of the leading part of the KAW perturbations is roughly equal to $4\ V_{A0}$, and that of the trailing part is about $1.8\ V_{A0}$. The convective flow speed $V_z \sim 2.0\ V_{A0}$ at the leading edge, where the local Alfvén speed is around 2–2.5 V_{A0}. Therefore, the speed of the leading part is about 80–90% of its local V_A in the wave frame, very close to the theoretical prediction based on Alfvén waves. The speed of the trailing part appears to be much smaller than the theoretically predicted speed, mainly because of the merging with newly-formed KAWs at the local magnetopause. In addition, note that the radial transmission of the foreshock compressional waves also leads to the resonance of closed field lines in the dipole field region [*Engebretson et al.*, 1987]. The global generation of Alfvén waves and the field line resonance in the outer magnetosphere has been discussed by *Lin and Wang* [2005] for a case similar to the one presented here.

[37] At $t = 164$, the north-south expansion of the circled region causes further weakened perturbations in the trailing part. In the circled region, the perturbations are seen deeper radially inside the outer magnetosphere. The leading part of the tracked KAW perturbations has propagated into the northern cusp region, where the wave patterns have reached $(x, z) = (3.5, 7.0)\ R_E$, as seen in Figure 12 (right column). Overall, pulses of newly-formed KAWs on the closed field lines continuously propagate into the cusp due to the self-consistent interaction of the magnetopause with foreshock waves.

4. Summary

[38] In summary, we have carried out a 3-D global hybrid simulation of mode conversion at the dayside magnetopause associated with the quasi-parallel shock. The mode conversion from compressional waves originating at the bow shock/foreshock to KAWs is investigated. The main results can be summarized as follows.

[39] 1. The wave structure, propagation, and time evolution in the 3-D magnetopause are presented. As the self-generated compressional wave structures propagate from the foreshock toward and impinge on the MPBL, strong $E_\parallel$ are excited during their interaction with the MPBL, together with the presence of correlated transverse perturbations in B_y, V_{iy}, and $J_\parallel$. These structures, with $k_\perp \rho_i \sim k_x \rho_i \sim 0.5$–1, are found to be KAWs due to the mode conversion process. The evolution of the KAWs leads to the generation of KAWs dominated by the azimuthal wave numbers k_y, consistent with the previous 3-D hybrid simulation of *Lin et al.* [2012] for mode conversion in a slab geometry of the MPBL.

[40] 2. The Alfvén mode test shows that the KAW structures satisfy the Alfvén wave polarization conditions. A spectral analysis for the wave modes dominated by k_y reveals that the dependence of transverse wave polarization of $E_y(k_y)/B_x(k_y)$ on the perpendicular wave number k_y is in agreement with the theoretical results for KAWs. The wave spectra of the strongly enhanced $E_\parallel$ for these modes also agree with those predicted by theories and previous simulations.

[41] 3. These KAW perturbations propagate poleward into the cusps along the MPBL, carrying the electromagnetic energy along field lines. Due to the differential flow convection speeds at various latitudes, the KAW packets expand along the north-south direction and may thus be weakened, while they may also merge with newly-formed KAWs due to newly-arrived compressional waves.

[42] 4. The mode conversion occurs in the MPBL due to the drastic increase of the local Alfvén speed V_A earthward. As the compressional waves approach the MPBL, the Alfvén resonance condition $\omega \simeq k_\parallel V_A$ is found to be satisfied at the increased V_A. The resulting KAWs are found to decay into the magnetosphere. The 3-D structures of correlated $E_\parallel$ and B_y are presented, indicating the spatial scales of KAWs from mode conversion process.

[43] 5. The power spectrum analyses of transverse and compressional components of the magnetic field reveal that the magnetosheath is abundant with compressional waves, while enhanced transverse waves appear around the MPBL region due to the mode conversion process.

[44] **Acknowledgments.** This work was supported by NASA grant NASA-NNX10AK97G and NSF grant ATM-0646442, ATM-0852682, and PHY-0903794 to Auburn University. Computer resources were provided by the Alabama Supercomputer Center (ASC) and NASA Advanced Supercomputing (NAS) Division.

[45] Masaki Fujimoto thanks Jay Johnson and Hiroshi Hasegawa for their assistance in evaluating this paper.

References

Anderson, B. J., S. A. Fuselier, S. P. Gary, and R. E. Denton (1994), Magnetic spectral signatures in the Earth's magnetosheath and plasma depletion layer, *J. Geophys. Res.*, *99*, 5877–5891.

Anderson, R. R., C. C. Harvey, M. M. Hoppe, and B. T. Tsurutani (1982), Plasma waves near the magnetopause, *J. Geophys. Res.*, *87*, 2087–2107.

Andre, M., A. Vaivads, and Y. V. Khotyaintsev (2010), Magnetic reconnection and cold plasma at the magnetopause, *Geophys. Res. Lett.*, *37*, L22108, doi:10.1029/2010GL044611.

Badman, S. V., and S. W. H. Cowley (2007), Significance of Dungey-cycle flows in Jupiter's and Saturn's magnetospheres, and their identification on closed equatorial field lines, *Ann. Geophys.*, *25*, 941–951.

Bellan, P. M. (2012), Improved basis set for low frequency plasma waves, *J. Geophys. Res.*, *117*, A12219, doi:10.1029/2012JA017856.

Blanco-Cano, X., N. Omidi, and C. T. Russell (2009), Global hybrid simulations: Foreshock waves and cavitons under radial interplanetary magnetic field geometry, *J. Geophys. Res.*, *114*, A01216, doi:10.1029/2008JA013406.

Bogdanova, Y. V., et al. (2004), Correlation between suprathermal electron bursts, broadband extremely low frequency waves, and local ion heating in the midaltitude cleft/lowlatitude boundary layer observed by cluster, *J. Geophys. Res.*, *109*, A12226, doi:10.1029/2004JA010554.

Chaston, C., et al. (2008), Turbulent heating and cross-field transport near the magnetopause from THEMIS, *Geophys. Res. Lett.*, *35*, L17S08, doi:10.1029/2008GL033601.

Chaston, C. C., C. W. Carlson, W. J. Peria, R. E. Ergun, and J. P. McFadden (1999), FAST observations of inertial Alfvén waves in the dayside aurora, *Geophys. Res. Lett.*, *26*, 647–650, doi:10.1029/1998GL900246.

Chaston, C. C., M. Wilber, F. S. Mozer, M. Fujimoto, M. L. Goldstein, M. Acuna, H. Reme, and A. Fazakerley (2007), Mode conversion and anomalous transport in Kelvin-Helmholtz vortices and kinetic Alfvén waves at the Earth's magnetopause, *Phys. Rev. Lett.*, *99*(17), 175,004, doi:10.1103/PhysRevLett.99.175004.

Chaston, C. C., J. W. Bonnell, L. Clausen, and V. Angelopoulos (2012), Correction to "energy transport by kinetic-scale electromagnetic waves in fast plasma sheet flows", *J. Geophys. Res.*, *117*, A12205, doi:10.1029/2012JA018476.

Chaston, C. C., et al. (2005), Energy deposition by alfvén waves into the dayside auroral oval: Cluster and fast observations, *J. Geophys. Res.*, *110*, A02211, doi:10.1029/2004JA010483.

Chen, L. (1999), Theory of plasma transport induced by low-frequency hydromagnetic waves, *J. Geophys. Res.*, *104*, 2421–2428.

Chen, L., and A. Hasegawa (1974), Plasma heating by spatial resonance of Alfvén wave, *Phys. Fluids*, *17*(7), 1399–1403.

Cheng, C. Z., and J. R. Johnson (1999), A kinetic-fluid model, *J. Geophys. Res.*, *104*(A1), 413–428, doi:10.1029/1998JA900065.

Clemmons, J. H., et al. (2000), Observations of traveling pc5 waves and their relation to the magnetic cloud event of January 1997, *J. Geophys. Res.*, *105*, 5441–5452, doi:10.1029/1999JA900418.

Engebretson, M. J., L. J. Zanetti, T. A. Potemra, W. Baumjohann, and H. Luhr (1987), Simultaneous observations of Pc 3-4 pulsations in the solar wind and in the Earth's magnetosphere, *J. Geophys. Res.*, *92*, 10,053–10,062.

Engebretson, M. J., L. J. Cahill, Jr., R. L. Arnoldy, B. J. Anderson, and T. J. Rosenberg (1991), The role of the ionosphere in coupling upstream ULF wave power into the dayside magnetosphere, *J. Geophys. Res.*, *96*, 1527–1542.

Fuselier, S. A., K. J. Trattner, and S. M. Petrinec (2000), Cusp observations of high- and low-latitude reconnection for northward interplanetary magnetic field, *J. Geophys. Res.*, *105*, 253–266, doi:10.1029/1999JA900422.

Hasegawa, A., and L. Chen (1974), Plasma heating by Alfvén-wave phase mixing, *Phys. Rev. Lett.*, *32*, 454–456, doi:10.1103/PhysRevLett.32.454.

Hasegawa, A., and L. Chen (1976), Kinetic processes in plasma heating by resonant mode conversion of Alfvén wave, *Phys. Fluids*, *19*, 1924–1934.

Hasegawa, A., and K. Mima (1978), Anomalous transport produced by kinetic Alfvén wave turbulence, *J. Geophys. Res.*, *83*, 1117–1123.

Hasegawa, A., K. H. Tsui, and A. S. Assis (1983), A theory of long period magnetic pulsations. III - Local field line oscillations, *Geophys. Res. Lett.*, *10*, 765–767.

Hasegawa, H., K. Maezawa, T. Mukai, and Y. Saito (2002), Plasma entry across the distant tail magnetopause 2. Comparison between MHD theory and observation, *J. Geophys. Res.*, *107*, SMP 6-1–SMP 6-8, doi:10.1029/2001JA900138.

Hollweg, J. V. (1999), Kinetic Alfvén wave revisited, *J. Geophys. Res.*, *104*, 14,811–14,819, doi:10.1029/1998JA900132.

Izutsu, T., H. Hasegawa, T. K. M. Nakamura, and M. Fujimoto (2012), Plasma transport induced by kinetic Alfvén wave turbulence, *Phys. Plasmas*, *19*, 102,305, doi:10.1063/1.4759167.

Johnson, J. R., and C. Z. Cheng (1997), Kinetic Alfvén waves and plasma transport at the magnetopause, *Geophys. Res. Lett.*, *24*(11), 1423–1426, doi:10.1029/97GL01333.

Johnson, J. R., and C. Z. Cheng (2001), Stochastic ion heating at the magnetopause due to kinetic Alfvén waves, *Geophys. Res. Lett.*, *28*(23), 4421–4424, doi:10.1029/2001GL013509.

Johnson, J. R., C. Z. Cheng, and P. Song (2001), Signatures of mode conversion and kinetic Alfvén waves at the magnetopause, *Geophys. Res. Lett.*, *28*(2), 227–230, doi:10.1029/2000GL012048.

Kajdic, P., X. Blanco-Cano, N. Omidi, and C. T. Russell (2011), Multi-spacecraft study of foreshock cavitons upstream of the quasi-parallel bow shock, *Planet. Space Sci.*, *59*, 705–714, doi:10.1016/j.pss.2011.02.005.

Lee, L. C., J. R. Johnson, and Z. W. Ma (1994), Kinetic Alfvén waves as a source of plasma transport at the dayside magnetopause, *J. Geophys. Res.*, *99*(A9), 17,405–17,411.

Lin, Y., and X. Y. Wang (2005), Three-dimensional global hybrid simulation of dayside dynamics associated with the quasi-parallel bow shock, *J. Geophys. Res.*, *110*, A12216, doi:10.1029/2005JA011243.

Lin, Y., and H. Xie (1997), Formation of reconnection layer at the dayside magnetopause, *Geophys. Res. Lett.*, *24*, 31–45.

Lin, Y., X. Y. Wang, and S.-W. Chang (2007), Connection between bow shock and cusp energetic ions, *Geophys. Res. Lett.*, *34*, L11107, doi:10.1029/2007GL030038.

Lin, Y., J. R. Johnson, and X. Y. Wang (2010), Hybrid simulation of mode conversion at the magnetopause, *J. Geophys. Res.*, *115*, A04208, doi:10.1029/2009JA014524.

Lin, Y., J. R. Johnson, and X. Y. Wang (2012), Three-dimensional mode conversion associated with kinetic Alfvén waves, *Phys. Rev. Lett.*, *109*, 125003, doi:10.1103/PhysRevLett.109.125003.

Nykyri, K., A. Otto, B. Lavraud, C. Mouikis, L. M. Kistler, A. Balogh, and H. Rème (2006), Cluster observations of reconnection due to the Kelvin-Helmholtz instability at the dawnside magnetospheric flank, *Ann. Geophys.*, *24*, 2619–2643.

Otto, A., and D. H. Fairfield (2000), Kelvin-Helmholtz instability at the magnetotail boundary: MHD simulation and comparison with Geotail observations, *J. Geophys. Res.*, *105*, 21,175–21,190, doi:10.1029/1999JA000312.

Phan, T. D., and G. Paschmann (1996), Low-latitude dayside magnetopause and boundary layer for high magnetic shear 1. Structure and motion, *J. Geophys. Res.*, *101*, 7801–7816, doi:10.1029/95JA03752.

Phan, T.-D., G. Paschmann, and B. U. Ö. Sonnerup (1996), Low-latitude dayside magnetopause and boundary layer for high magnetic shear 2. Occurrence of magnetic reconnection, *J. Geophys. Res.*, *101*, 7817–7828, doi:10.1029/95JA03751.

Rezeau, L., A. Morane, S. Perraut, A. Roux, and R. Schmidt (1989), Characterization of Alfvenic fluctuations in the magnetopause boundary layer, *J. Geophys. Res.*, *94*, 101–110.

Russell, C. T., and R. C. Elphic (1978), Initial ISEE magnetometer results: Magnetopause observations, *Space Sci. Rev.*, *22*, 681–715, doi:10.1007/BF00212619.

Russell, C. T., and R. C. Elphic (1979), Isee observations of flux transfer events at the dayside magnetopause, *Geophys. Res. Lett.*, *6*, 33–36, doi:10.1029/GL006i001p00033.

Song, P., C. T. Russell, R. J. Fitzenreiter, J. T. Gosling, M. F. Thomsen, D. G. Mitchell, S. A. Fuselier, G. K. Parks, R. R. Anderson, and D. Hubert (1993), Structure and properties of the subsolar magnetopause for northward interplanetary magnetic field - Multiple-instrument particle observations, *J. Geophys. Res.*, *98*, 11,319–11,337.

Southwood, D. J. (1974), Some features of field line resonances in the magnetosphere, *Planet. Space Sci.*, *22*, 483–491.

Stasiewicz, K., C. E. Seyler, F. S. Mozer, G. Gustafsson, J. Pickett, and B. Popielawska (2001), Magnetic bubbles and kinetic Alfvén waves in the high-latitude magnetopause boundary, *J. Geophys. Res.*, *106*(A12), 29,503–29,514.

Streltsov, A. V., W. Lotko, J. R. Johnson, and C. Z. Cheng (1998), Small-scale, dispersive field line resonances in the hot magnetospheric plasma, *J. Geophys. Res.*, *103*, 26,559–26,572.

Swift, D. W. (1996), Use of a hybrid code for a global-scale plasma simulation, *J. Comput. Phys.*, *126*, 109–121.

Tamao, T. (1965), Transmission and coupling resonance of hydromagnetic disturbances in the non-uniform Earth's magnetosphere, *Sci. Rep. Tohoku Univ., Ser. 5, Geophys.*, *17*(2), 43–54.

Tan, B., Y. Lin, J. D. Perez, and X. Y. Wang (2012), Global-scale hybrid simulation of cusp precipitating ions associated with magnetopause reconnection under southward IMF, *J. Geophys. Res.*, *117*, A03217, doi:10.1029/2011JA016871.

Tsurutani, B. T., and R. M. Thorne (1982), Diffusion processes in the magnetopause boundary layer, *Geophys. Res. Lett.*, *9*, 1247–1250, doi:10.1029/GL009i011p01247.

Uberoi, C. (1972), Alfvén waves in inhomogeneous magnetic fields, *Phys. Fluids*, *15*, 1673–1675.

Wang, C.-P., L. R. Lyons, T. Nagai, J. M. Weygand, and R. W. McEntire (2007), Sources, transport, and distributions of plasma sheet ions and electrons and dependences on interplanetary parameters under northward interplanetary magnetic field, *J. Geophys. Res.*, *112*, A10224, doi:10.1029/2007JA012522.

Wang, X. Y., Y. Lin, and S.-W. Chang (2009), Hybrid simulation of foreshock waves and ion spectra and their linkage to cusp energetic ions, *J. Geophys. Res.*, *114*, A06203, doi:10.1029/2008JA013745.

Yao, Y., C. C. Chaston, K. Glassmeier, and V. Angelopoulos (2011), Electromagnetic waves on ion gyro-radii scales across the magnetopause, *Geophys. Res. Lett.*, *38*, L09102, doi:10.1029/2011GL047328.